




# Solid state dewetting of a metal –semiconductor bi-layers deposited onto c-Si substrate

S. Halindintwali<sup>1,\*</sup> , M. Masenya<sup>2</sup>, M. Madhuku<sup>2</sup>, C. Mtshali<sup>3</sup>, F. Cummings<sup>1</sup>, and C. Oliphant<sup>4</sup>

<sup>1</sup>Physics Department, University of the Western Cape, Private Bag X17, Bellville 7535, South Africa

<sup>2</sup>TAMS Laboratory, iThemba LABS, Private Bag 11, Johannesburg 2050, South Africa

<sup>3</sup>Tandetron Laboratory, iThemba LABS, PO Box 722, Somerset West, Cape Town 7129, South Africa

<sup>4</sup>National Metrology Institute of South Africa, Private Bag X34, Lynnwood Ridge, Pretoria 0040, South Africa

Received: 30 November 2022

Accepted: 17 February 2023

Published online:  
20 March 2023

© The Author(s) 2023

## ABSTRACT

A bi-layers stack consisting of a semiconductor thin film of a varied thickness and a very thin Pd layer (SiC/Pd/c-Si) was deposited onto c-Si by e-beam evaporation at room temperature. The multi-layers structure was subjected to a thermal annealing process at near eutectic temperature of the Si – Pd phase. It is noticed, through top view SEM and cross-section STEM analyses, that the sandwiched Pd metal layer dewets from the interface with the c-Si substrate in well dispersed nanoparticles and it diffuses inward onto the top few monolayers of the substrate; at times it permeates shallowly through the SiC semiconductor top layer. The size distribution of the nanoparticles was found to be closely linked to the thickness of the top semiconductor layer. On the other hand, the top SiC layer was found to form islands protruding above the surface, when the film was very thin. When thicker, the semiconductor SiC layer retained its integrity and remained unaffected. An optical model of the resulting metal-dielectric mixed layer is proposed.

## 1 Introduction

Thin metal films deposited on non-metal substrates like ceramics and semiconductors have been reported to be thermodynamically metastable and to dewet from the substrate surface through solid state diffusion at sufficiently high temperature of annealing, even below the melting point of the material [1, 2]. Although SSD of thin films has been considered in the past to be harmful to thermal and electronic

transport in microsystems, it has now also emerged as a beneficial way of controlling the nanostructures growth [3, 4] for varied applications. Hence the motivation to investigate on its mechanisms and kinetics [5], especially in multilayers structure. Although a large body of knowledge has now been accumulated on the mechanism behind the dewetting of one single metal layer and single thin crystalline films on a substrate [6–9], SSD of bi- and multilayers adds more complexity to the SSD problem of pure

Address correspondence to E-mail: shalindintwali@uwc.ac.za

metals as the intermixing of individual sub-layers happens on a different timescale [10] and it is not well understood; yet the SSD of multilayers represents a simple fabrication method of supported nanoparticles with tunable composition and functional properties [11, 12]. Mamogo et al. [13] have recently discussed the effect of SSD of thin metal layer on an intercalated semiconductor between the dewetted metal and the substrate. A “c-Si substrate/SiC layer/thin Pd metal” structure was used in that study. It was shown that, at a temperature of annealing close to the eutectic point of the Pd/Si phase, the Pd metal upon dewetting, was diffusing inward into the SiC layer. In this study, we want to investigate the structure “Substrate/Metal/Semiconductor” namely “c-Si/Pd/SiC” for its dewetting mechanism and for the optical properties of the SiC layer upon annealing. The binary compound SiC is a promising semiconductor for applications in optoelectronics, sensing and energy due to its outstanding properties such as a wide bandgap, a high phonon frequency, a high thermal conductivity and breakdown voltage [2, 14–16]. For an homogeneous semiconductor layer like a-Si:H or a-SiC:H on a substrate, it is easy to obtain the optical constants [17–20] from the reflection and transmission spectra as long as they have a reasonable number of interference fringes. In the studied layers stack, a composite semiconductor-metal is obtained upon dewetting of the thin metal layer; not only the layer is inhomogeneous but also the spectra studied do not display a sufficient number of extrema of interference, there is thus a need to devise accurate optical models for such mixed phase composite, taking into account the effective dielectric function.

## 2 Experimental techniques

A palladium thin film of a 5 nm fixed thickness and a SiC layer of varied thicknesses were deposited onto n-doped (100) c-Si substrate using high vacuum electron beam evaporation at room temperature. The cleaning procedure of the substrate and the deposition details of the samples have been reported elsewhere [13]. After the deposition, the samples were annealed in a chamber maintained at a pressure of  $1 \times 10^{-7}$  mbar at 800 °C for periods ranging from 1 to

6 h. The temperature was ramped from room temperature to 800 °C at a rate of 25 °C/min. When the required temperature was reached, the chamber was kept at 800 °C for the annealing duration. Thereafter, the furnace was allowed to cool down to room temperature overnight. For the scanning electron microscopy studies (SEM), a Zeiss Auriga field-emission gun scanning electron microscope (FEG-SEM) was used for characterization of the surface morphology and elemental composition of the films. It was operated at 5 kV for imaging using an Everhart-Thornley secondary electron detector and at 20 kV for energy dispersive X-ray spectroscopy (EDX) analysis using an Oxford Instruments X-Max solid-state silicon drift detector. In the focussed ion beam, the data were acquired on a Zeiss Cross Beam 540 operated at 5 kV using the in-lens and EsB detectors. The in-lens provides high resolution secondary electron images while the EsB detector provides high resolution atomic number contrast. The EDS data (X-ray maps and Point ID) were acquired on an Oxford X-Max Extreme ‘windowless’ detector operated in the same conditions. The TEM studies were done using a Technai G220 field emission gun transmission electron microscope (FEG-TEM), operated in scanning transmission electron microscopy (STEM) mode. The images were acquired at 200 kV accelerating voltage. Raman spectroscopy: was carried out by a WITec alpha 300 RAS + confocal Raman microscope using a laser wavelength of 532 nm at a power of ~5 mW. The Raman z-scan images were collected on a width of 15  $\mu\text{m}$  and depth of 10  $\mu\text{m}$ . 200 lines per image were scanned over an integration time of 1 second. Fourier transform infrared (FTIR) analysis was conducted using a perkin Elmer Spectrum 100, in the range 400–4000  $\text{cm}^{-1}$  for molecular vibrational studies. The reflection (R) spectra in the visible region of the spectrum were obtained by a Maya 2000 PRO spectrometer, a product of Ocean Insight, and the R spectra were modelled using SCOUT software [21]. Two layer stacks, one consisting of 10 nm SiC/5 nm Pd/c-Si and the other of 40 nm SiC/5 nm Pd/c-Si were investigated in this study. Although surface morphology and structural studies are done on samples annealed at 800 °C where the dewetting was observed, samples annealed at 800 °C are contrasted with those annealed at a lower temperature of 500 °C in order to study the evolution of optical constants.

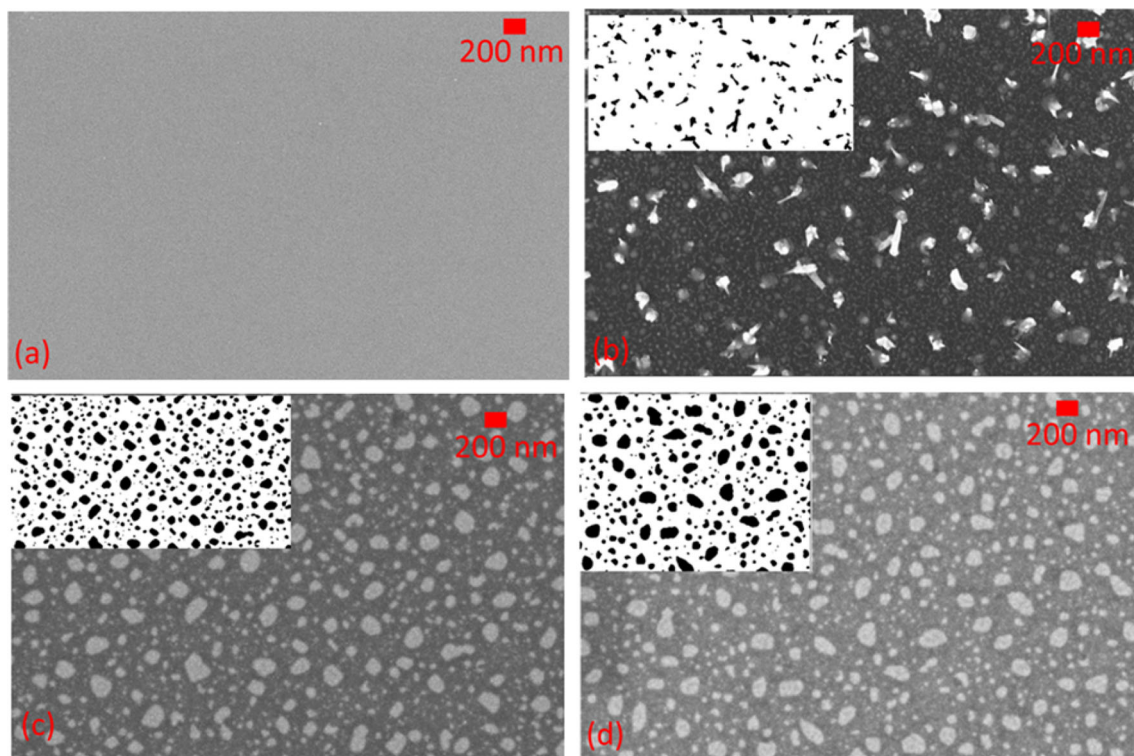
### 3 Results and discussion

#### 3.1 Surface morphology

Figure 1 shows the surface morphology of the layer stack with structure 10 nm SiC/5 nm Pd/c-Si substrate in as-deposited (a) and annealed state (b–d); the inserts on the left top corner of micrographs from annealed samples are the respective FFT bandpass filtered images, as generated from Image J software. Figure 1a displays the SEM in-lens micrograph of the pristine sample which is clearly characterized by a smooth surface. Figure 1b–d show the micrographs of the same stack annealed at 800 °C for 1 h, 2 and 3 h respectively. The surface morphology of the sample annealed for a shorter period in (b) reveals the growth of nano-needle & rod like structures of different shapes and randomly orientated; this can still be considered as the initial stage of dewetting of the palladium film at the interface with the c-Si substrate. Prolonged annealing in (c, d) results in more defined, but at times distorted nanosphere features. This results from the minimization of the surface energy

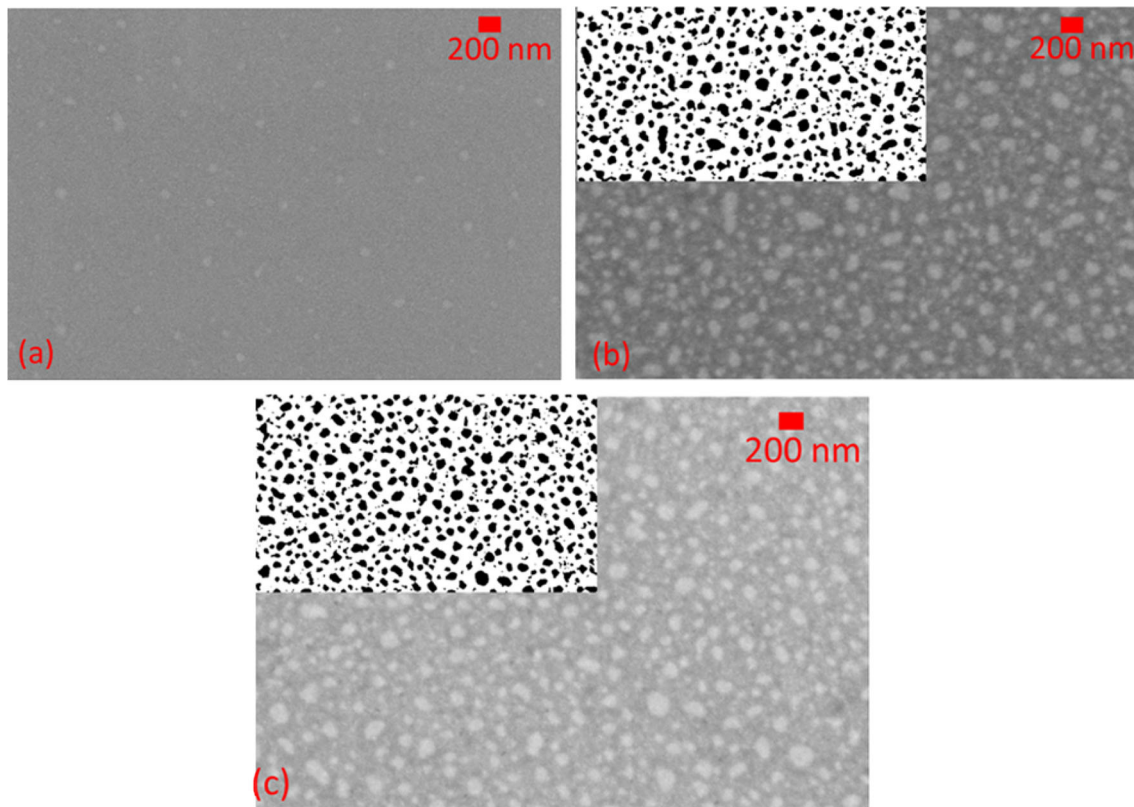
as more and more of the rod-features take spherical shape and increase in volume.

Figure 2 presents the SEM micrographs of the 40 nm SiC/5nm Pd/c-Si layers stack where (a) is from the as deposited sample, (b) from the annealed sample at 800 °C for 1 h and (c) from the 800 °C annealed sample for 3 h. In contrast to the pristine stack of Fig. 1a, the as-deposited layers stack in Fig. 2a shows already the presence of mono-dispersed small nano-dots; it is unclear at this stage if, during deposition, the top relatively thick SiC layer exerted much stronger interfacial forces to the thin Pd film forcing it to disperse in small droplets. After one hour of annealing, as shown by the nano-structural details in Fig. 2b, nano-spherical features appear in greater density when compared to the micrograph of the stack in Fig. 1b with the same conditions of annealing but where a top thinner SiC layer was used. It appears thus that a thermal stability of the bilayer was reached faster in the stack with a thicker SiC surface layer. There is no major difference between the microstructure between the micrographs in Fig. 2b and Fig. 2c where different times of



**Fig. 1** Dewetting of the 10 nm SiC film/5 nm Pd thin film/c-Si substrate stack: **a** the pristine structure; **b** the SEM in-lens micrograph of the same layers stack annealed at 800 °C for one

hour; **c** the same layers stack annealed for two hours and **d** the same stack annealed for three hours



**Fig. 2** Dewetting of the 40 nm SiC film/5 nm Pd thin film/c-Si substrate stack: **a** In-lens SEM micrograph of the pristine structure; **b** the same layers stack annealed at 800 °C for one hour and **c** the same layers stack annealed for three hours

annealing were used. The same observation holds for Fig. 1c and Fig. 1d. We propose thus that the dewetting process in these bilayers structures is more sensitive to the thickness of the semiconductor when the thermal stability of the bilayer has been achieved. Furthermore, in comparing Fig. 1b, c and Fig. 2b, c, it can be observed that the dewetting is more sensitive to the thickness of the top layer but less sensitive to the annealing time in both cases.

Figures 3 and 4 show the size distribution of the dewetted nanoparticles for the two stacks discussed in Figs. 1 and 2 respectively, as measured using ImageJ software. The average crystal size values are appended on the figures. As the microstructure of the stack 10 nm SiC/ 5 nm Pd / c-Si annealed for 1 h had shown planar and rods looking features rather than spherical ones (please refer to Fig. 1b), the “diameter” label would be misleading; one needs to understand “size” for this particular sample as a length measured in the confined dimension. However the size labeling approximates the diameter of the nanoparticles for the other column-bar plots. A general observation is that the distributions point to small islands

coarsening into isolated spherical –like larger particles. This can be explained in terms of interfacial energy minimization. No particles agglomeration was observed; we hypothesize that the SiC layer on top of the dewetting Pd thin film acts a capping / encapsulating layer on the formed nanoparticles offering a thermal and physical barrier against agglomeration especially when the top SiC film was grown conformal and thicker.

The effect of the encapsulating layer and its thickness is demonstrated much more clearly by the High-angle annular dark field (HAADF) micrographs of the lamellae (prepared for TEM studies) imaged by the FIB SEM in Fig. 5. The inserts on the left top corner of the micrographs are the respective FFT bandpass filtered images, as generated from Image J software. For the orientation of the reader, it is important to note that before FIB sectioning, a thin C layer of less than 100 nm was deposited by e-beam followed by a thick gas-injected C layer of about 1  $\mu\text{m}$  in order to protect the bilayer of interest. Figure 5a shows the SEM micrograph of the lamella prepared from 10 nm SiC/ 5 nm Pd /c-Si stack. It is observed



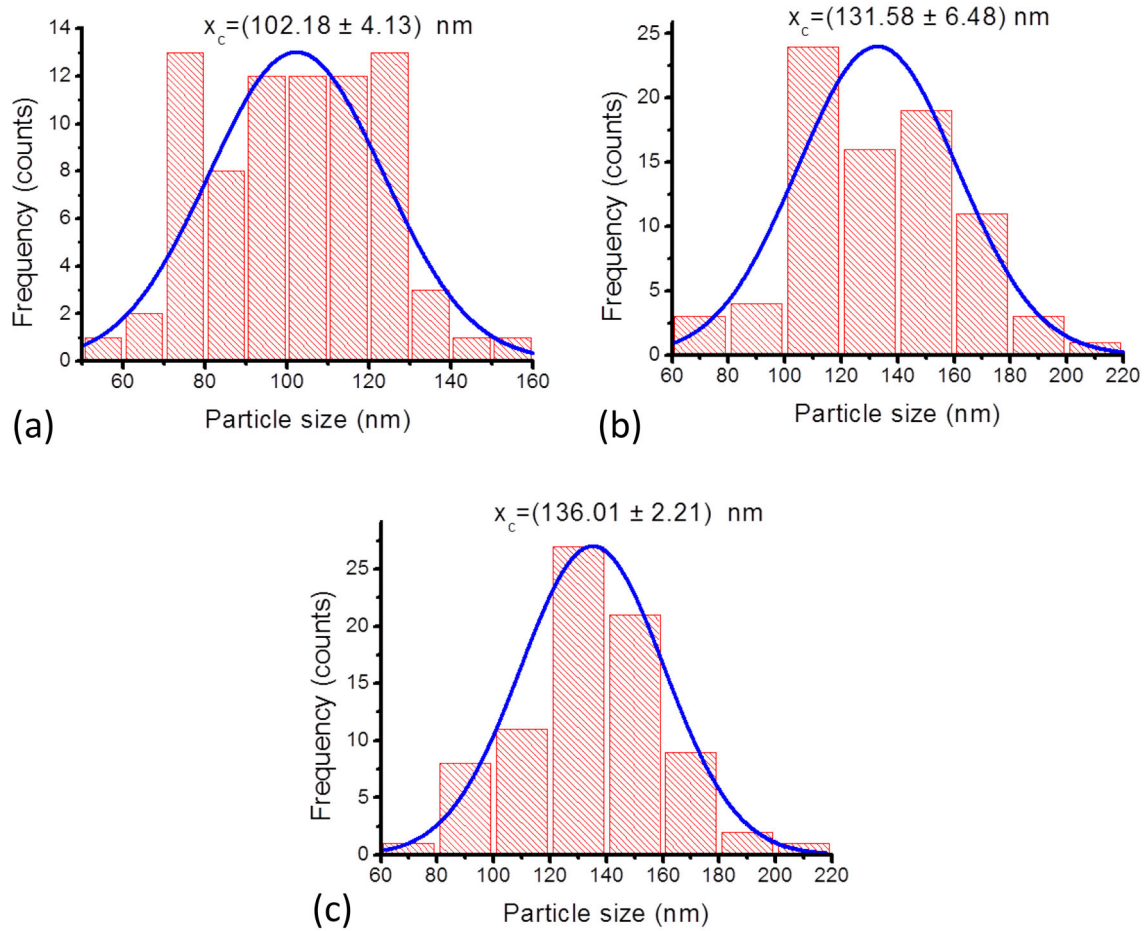


**Fig. 3** Size distribution of the dewetted nanoparticles in the 10 nm SiC/ 5 nm Pd / c-Si stack after the annealing treatment at 800 °C for **a** 1 h; **b** 2 h and **c** 3 h

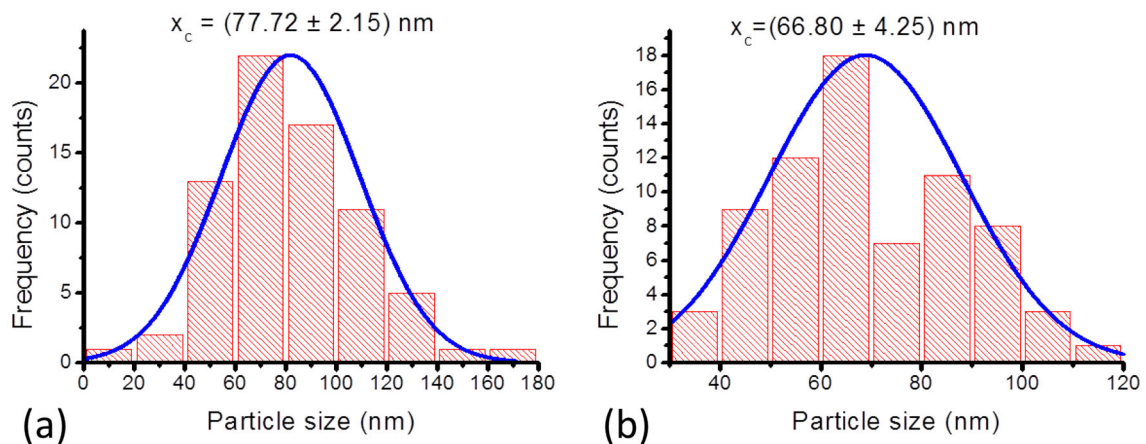


**Fig. 4** Size distribution of dewetted nanoparticles in the 40 nm SiC/ 5 nm Pd / c-Si stack after the annealing treatment at 800 °C for **a** one hour and **b** for 3 h

that the Pd thin layer dewetted and formed half-hemisphere looking features protruding into the interfacial layer of c-Si substrate; we noticed also that

the Pd layer and the top SiC film intermixed to give bright distinguishable Pd nanoparticle embedded into a dark grey matrix. The Pd-Si phase diagram [22]

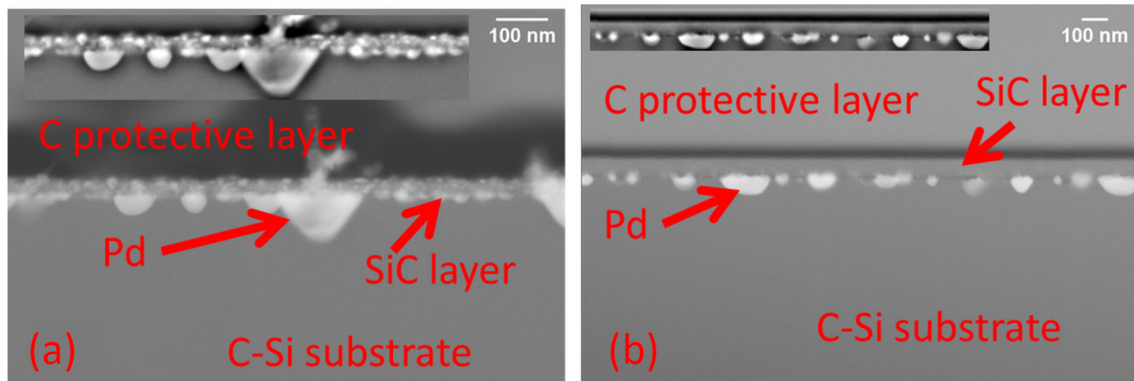


**Fig. 5** HAADF micrographs acquired by the FIB SEM **a** 10 nm SiC/ 5 Pd/ c-Si with a top deposited C protective layer ; **b** 40 nm SiC/5 Pd/c-Si with a top deposited C protective layer. The inserts are the corresponding FFT images

shows that at the lowest eutectic temperature of around 800 °C; metal rich silicide is formed with a Si solubility of less than 20 at%; Si rich silicide also do form but at a higher temperatures than the one used in this study. On the other hand, the Pd-C diagram phase diagram [22] shows that the solubility of C is very small and it has been reportedly to be only 0.02% by weight at 1700 °C [23]. The interfacial reactions between the SiC and noble metals like Pd result thus in silicide and a free C as no metal carbide is formed. The observed dark grey phase observed in Fig. 5a comprises of silicide and C precipitates that eventually evolve in C clusters. The half-hemisphere bright nanoparticles, seen brighter due to Z contrast, are Pd rich and are due to fast diffusion of the dewetted material inward, the top layer being already supersaturated.

Figure 5b is generated from a similar stack as in Fig. 5a where the 10 nm SiC layer is replaced by a 40 nm SiC thicker one. In contrast to Fig. 5a, the top SiC layer is still intact after the clear dewetting of the sandwiched Pd layer. This can be explained by the growth of a conformal semiconductor layer that do not avail any diffusion path but instead acts as a barrier encapsulating layer as explained above. We can thus consider that the growth of this dispersed Pd nanoparticles at the interfaces with both the substrate and the SiC top layer is driven by the minimization of the volume energy while the surface energy is negligible. The results discussed above are corroborated by the scanning TEM and the elemental X-ray mapping analysis in Fig. 6.

The STEM HAADF image on the top left corner shows in bright white font the dewetted Pd nanoparticles in SiC(10 nm)/Pd(5 nm)/c-Si layer

stack; the most prominent large one is clearly encroaching in the c-Si substrate while the smaller ones are intermixed with the top SiC layer. The X-ray map of Si (in green) shows a distinctive shadow of this large Pd particle. The image in a yellow colour code on the top panel shows much clearer the areal distribution of the Pd nanoparticles. Finally the image in the blue colour code represent the area map of C; it has to be emphasized here that most of the C signal is coming from the protective layer, as mentioned earlier a thin protective C layer was deposited by e-beam, followed by a thick gas-injected C layer before the FIB sectioning process. An analogue analysis can be done about the images of the bottom panel that represent the SiC(40 nm)/Pd(5 nm)/c-Si layer stack; the highlights here is that on the right bottom STEM image, the thick SiC layer has maintained its integrity and the Pd dewetted nanoparticles are isolated from each other. At the same time on the Si map (2nd bottom right), more shadows of Pd can be seen in the sub-interface region.

### 3.2 Structural analysis

Figure 7 presents typical confocal Raman results as obtained from the as deposited 10 nm SiC/5 nm Pd/ c-Si layer stack. The optical image (a) displays the line scan running over two distinct contrasted regions; the depth Raman image in (b) shows them with two different colour codes (red and cyan) on top of the blue continuous substrate signal. The spectra (c) and (d) represent the respective average spectra obtained over the scanned depth. The spectrum in (c), emanating from the red colour code, shows mainly the characteristics of the c-Si with a prominent peak at

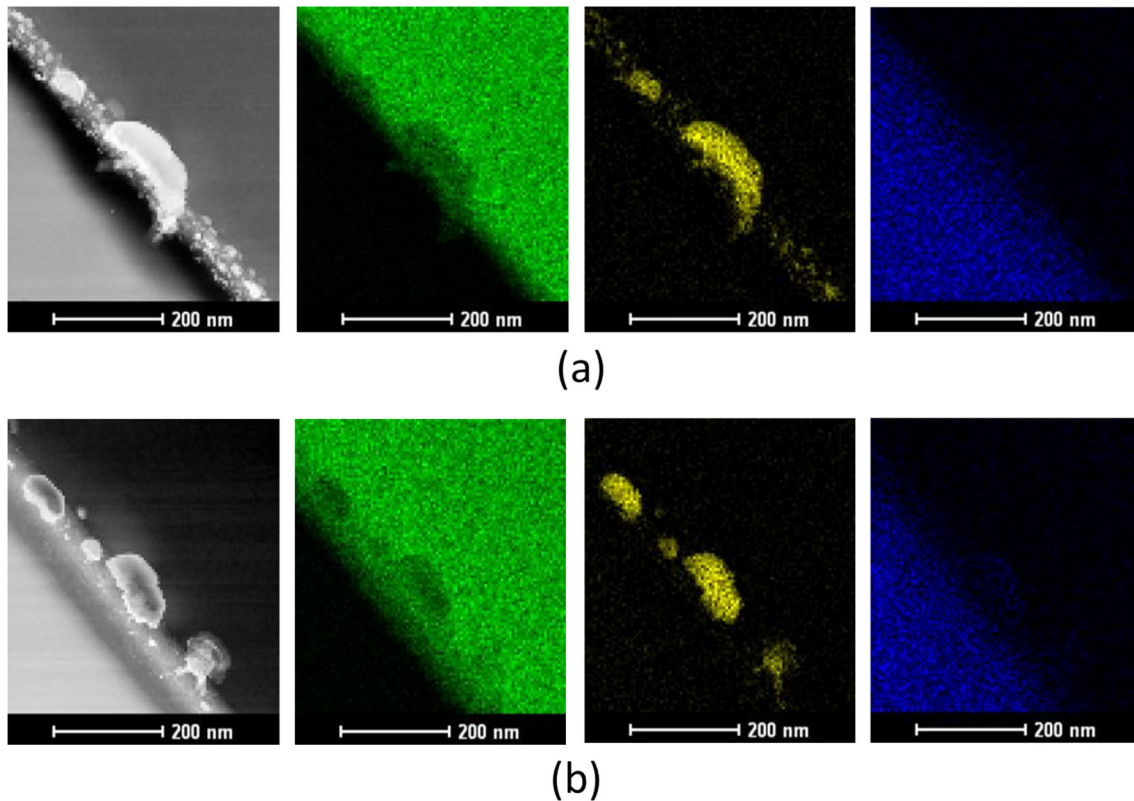


**Fig. 6** STEM images and elemental X-ray maps **a** top panel images: STEM HAADF micrograph on the top left and X-ray maps Si-K (green), Pd-L (yellow) and C-K (blue) imaged from SiC(10 nm)/Pd(5 nm)/c-Si layer stack; **b** the images of the bottom

panel convey the same information and in the respective colour code but they are taken from SiC(40 nm)/Pd(5 nm)/c-Si layer stack (Color figure online)

around  $520\text{ cm}^{-1}$  due to Si-Si TO vibration mode. The spectrum in (d), emanating from the cyan colour code, suggests that it is collected from a depth comprising also the deposited SiC film; in addition to the c-Si signal, we observe two peaks at around  $1400\text{ cm}^{-1}$  and at around  $1600\text{ cm}^{-1}$ ; they are due to C-C graphitic bonds, D- and G-bonds respectively.

In order to study the structural changes induced by annealing, Fig. 8 shows analogue analysis done on the same sample that was annealed one hour; it corresponds to Fig. 1b discussed earlier. The spectra (c) and (d) obtained from the two contrasted phases, green and red colour codes in (b), still all show the signal of the c-Si substrate. This is expected as the probed depth is  $10\text{ }\mu\text{m}$  as mentioned earlier in the experimental section.

The D-and G-graphitic bonds are still observed although they are more refined in the spectrum emanating from the surface region in green colour code; it might be that the bottom phase in red colour code has been affected by the mixing with the Pd

layer. Two additional peaks have been observed at around  $300\text{ cm}^{-1}$  and  $1000\text{ cm}^{-1}$ ; they correspond to SiC longitudinal optical (LO) and Si-Si longitudinal acoustic (LA) modes respectively. While the  $300\text{ cm}^{-1}$  suggests an amorphous Si (a-Si) disordered phase, the higher wavenumber at  $1000\text{ cm}^{-1}$  is attributed to the rearrangement of Si and C into bonded SiC [24]. The blue shift of the LO SiC normally expected at  $960\text{ cm}^{-1}$  is attributed to tensile strain due to the positive volume change of the crystal [25]. The field distortion may result from both Pd mixing and from the C clusters. The microstructure evolution has been also studied by FTIR; Fig. 9 plots the FTIR spectra collected from the 40 nm SiC/5 nm Pd/c-Si stack in its pristine state and in the annealed states for 1 and 2 h at  $800\text{ }^{\circ}\text{C}$ . Although the spectra were collected over a broad wavenumber range, our focus here is between  $700\text{ cm}^{-1}$ – $800\text{ cm}^{-1}$  where SiC gives an intense signal in infrared region. We notice that for as deposited stack (bottom spectrum in black colour font), Si and C are mainly



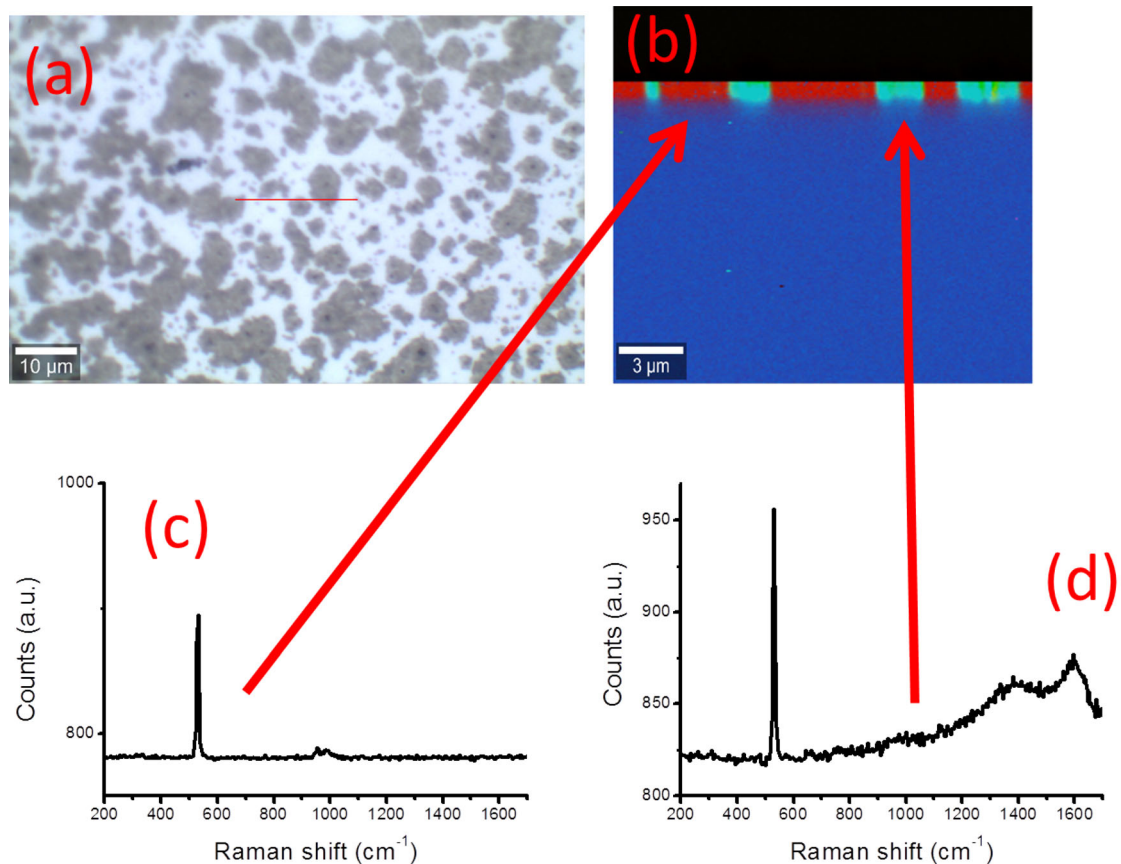


**Fig. 7** Raman analysis on the as-deposited 10 nm SiC/5 nm Pd/c-Si layer stack **a** optical image where the line scan is appended in red font colour; **b** depth Raman image where the colour codes

represent contrasting microstructures; **c** and **d** average Raman spectra corresponding to the two contrasted colour codes as indicated by the red arrows

bonded to oxygen; and after the thermal treatment (top spectra in blue and red colour fonts), it can be seen that Si and C are bonded as shown by the appearance of the prominent stoichiometric SiC TO vibration mode at around  $800\text{ cm}^{-1}$ . A broad Si-O stretching mode is also observed at around  $1100\text{ cm}^{-1}$ .

### 3.3 Optical analysis

As the SiC layer in the studied stacks was too thin to display consistent interference fringes that can be used to extract the optical constants by means of the interferometric equation. [17, 18], we have used SCOUT [21] to construct optical models that reproduced the measured reflection spectra. Four steps were performed in setting up the optical model and fitting the theoretical model to the experimental measured spectra. The first step consists in defining the “materials”; these are objects where optical

constants are defined over a given spectral range of investigation. Materials can be imported from the database or they are set from scratch. The second step consists in constructing the layers stack; this is a geometric structure where the layers are filled with the materials as pre-defined or imported from the database. The third step consists in defining the simulated spectra; a theoretical spectrum is generated and it will be fitted to the measured spectrum. The final step consists in fitting the parameters i.e. to adjust the model while fitting the experimental data. In order to set up the layer stack, the prior microstructure studies done constitute good tools to use in order to assume realistic layers to model. For instance in our case, since SiC had different stoichiometry sample by sample (please refer to Figs. 5 and 6), we assumed a concentration gradient where the SiC volume fraction would vary in the Si matrix. As oxidation bonds were found in the films in the above prior studies e.g. FTIR, we have introduced a



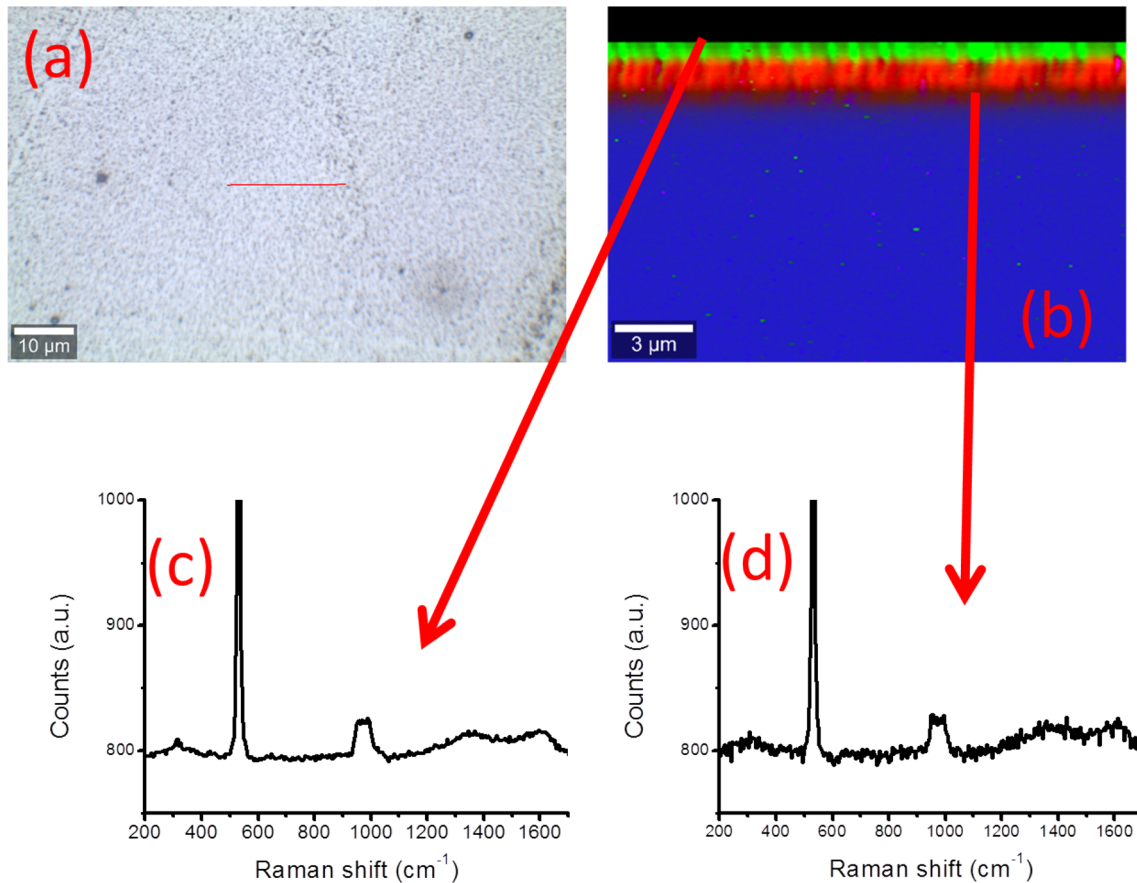


**Fig. 8** Raman analysis on the annealed 10 nm SiC/5 nm Pd/c-Si layer stack for 1 h **a** optical image where the line scan is appended in red font colour; **b** depth Raman image where the colour codes

represent contrasting microstructures; **c** and **d** average Raman spectra corresponding to the two contrasted colour codes as indicated by the red arrows

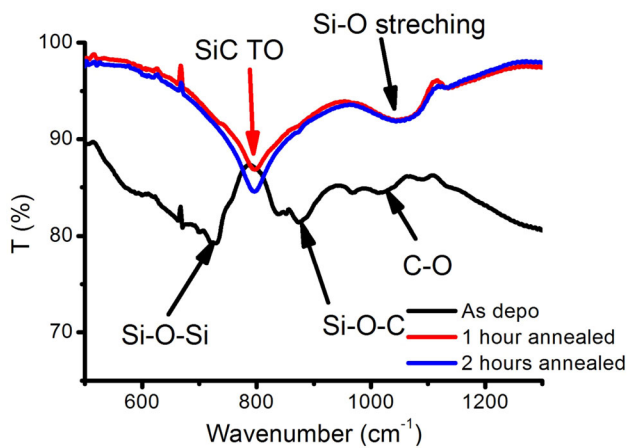


**Fig. 9** FTIR spectra of the 40 nm SiC/5 nm Pd/c-Si stack, as deposited and annealed for 1 and 2 h at 800 °C. The spectra are identified on the respective plots (Color figure online)

shallow layer of SiO<sub>x</sub> in the stack. While we kept Pd film as a single unmixed layer in as-deposited stack, we adopted a metal silicide in the annealed spectra.

The choice of the dielectric background of the material is a very important step as it determines de facto the fitting parameters. In order to get the right shape of the refractive index, a constant  $n_0$  was assumed in the long wavelength for the real part of the complex refractive index and an inter-band harmonic oscillator was chosen for normal dispersion of the refractive index. Another inter-band harmonic oscillator was adopted for bandgap absorption in semiconductor materials. Figure 10 shows the reflection spectra of the 40 nm SiC/5 nm Pd/c-Si stack as deposited and annealed at 500 °C and 800 °C for 1 h. The obtained simulated spectra are overlaid to the experimental ones. The deviation between the experimental and the simulation spectra must be minimized and it was found to be less than  $1 \cdot 10^{-5}$  in each case.

Figure 11 shows the dispersion relation obtained in terms of the real part of the refractive index as well as the absorption coefficients for the 500 °C and 800 °C annealed samples in red and black font respectively.

It is evident that the refractive index shows the expected normal dispersion upon an inter-band transition in the UV region. The obtained absorption coefficient can be used to calculate the energy gap using the Tauc model [19]. Figure 12 shows the extracted properties as function of annealing temperature from the proposed model for the SiC top layer of the stack. The increase of the SiC volume fraction within the Si matrix explains the obtained increasing values of the gap energy while the increase of the oxygen content with the increase of the annealing temperature justifies the decreasing trend of  $n_0$ .

## 4 Conclusion

The mechanism of dewetting of a noble Pd thin film metal sandwiched between a SiC semiconductor layer of varied thicknesses and a c-Si substrate was studied. Intermixing of the sandwiched noble metal

with the top semiconductor layer is observed when the thickness of the semiconductor layer was thin enough. As the solubility of Si is limited in Pd rich silicide and that no Pd carbide is expected according to both Pd-Si and Pd-C phase diagrams respectively, the non-intermixed dewetted Pd diffused towards the substrate where they thermally stabilize in semi-hemisphere features. When the top semiconductor is grown much thicker than the sandwiched metal layer, it is observed to act as a barrier layer to the metal that dewet towards the substrate. The conformal top semiconductor layer stayed unaffected. We have proposed an optical model through SCOUT that reproduced the measured spectra with deviations between measured and simulated spectra of less than  $1 \cdot 10^{-5}$  and giving at the same time the expected shape of the dielectric functions.

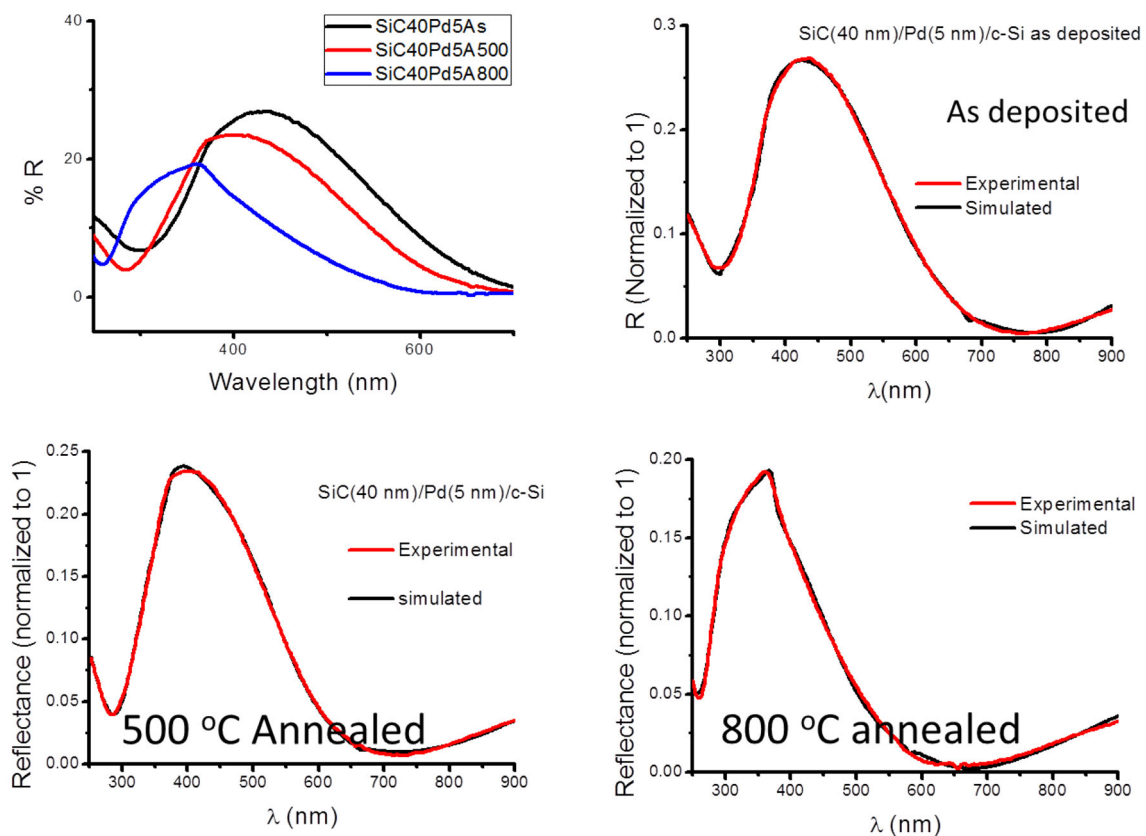


**Fig. 10** Experimental and simulated reflection spectra of as-deposited and annealed 40 nm SiC/5 nm Pd/c-Si stack at 500 °C and 800 °C for 1 h (Color figure online)

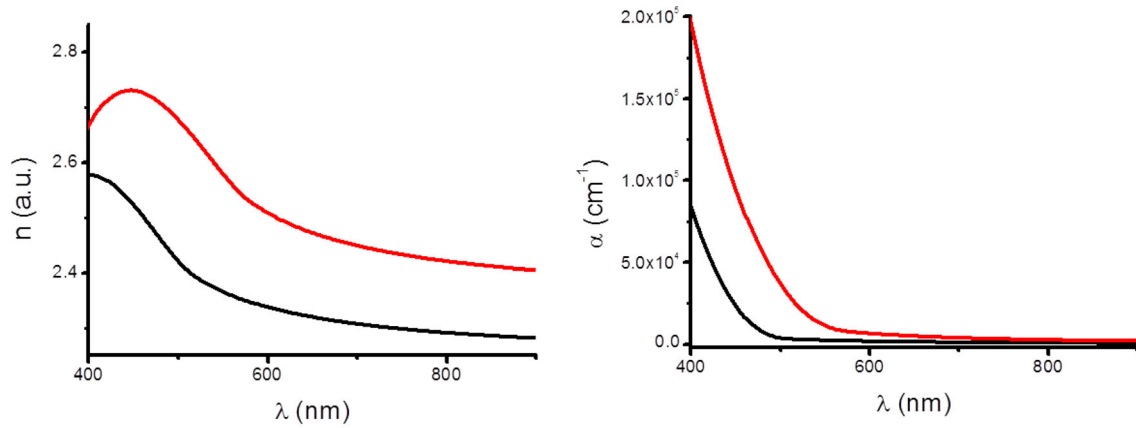


**Fig. 11** The simulated real part refractive index  $n(\lambda)$  and absorption coefficient  $\alpha(\lambda)$  of the annealed 40 nm SiC/5 nm Pd/ c-Si at 500 °C (red) and 800 °C (black) for 1 h (Color figure online)

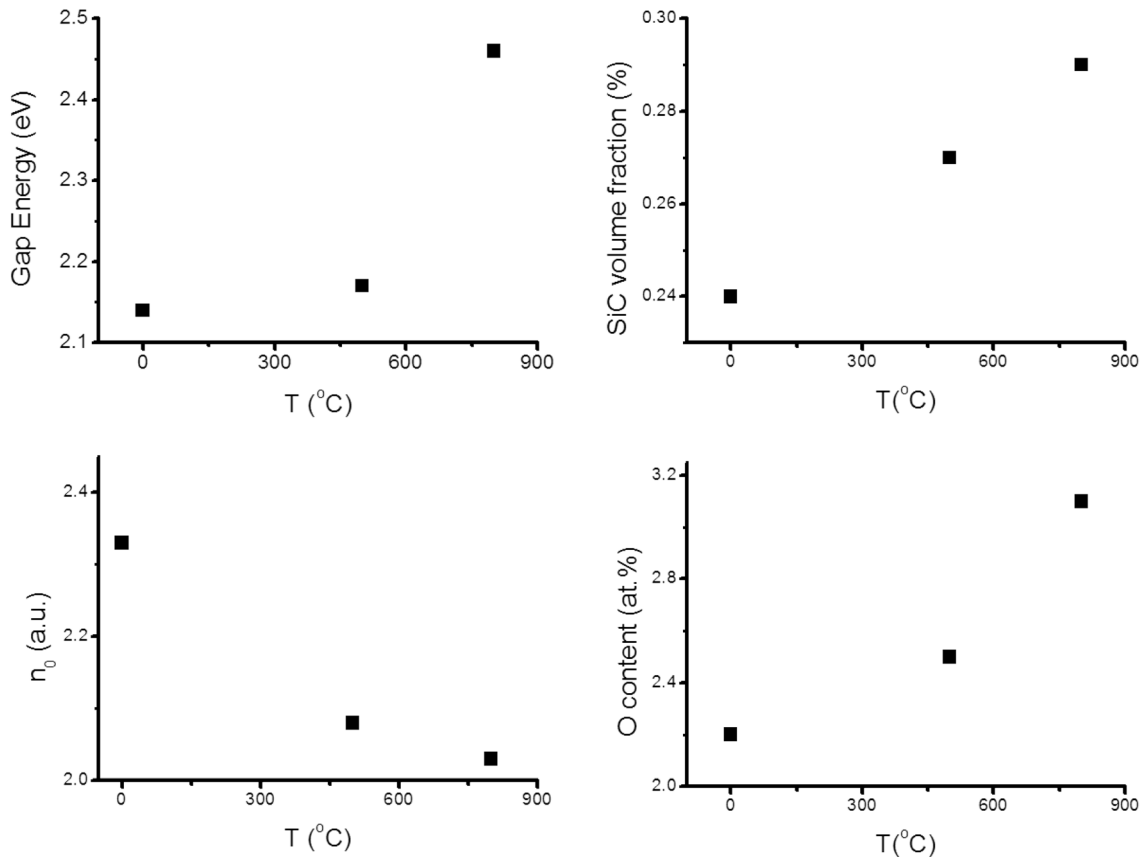


**Fig. 12** Extracted properties from the model for the SiC layer in the as-deposited layer stack and in the stacks annealed at 500 °C and 800 °C: Top panel for gap energy and SiC volume fraction and bottom panel for  $n_0$  and oxygen atomic content in the layer

### Acknowledgements

The corresponding author acknowledges the Research Office at the University of the Western Cape

for funding the face to face attendance to the 9th International Conference on Optical, Optoelectronic and Photonic Materials and Applications.



## Author contributions

SH, MM and MM contributed to the study conception and design. Material preparation, data collection and analysis were performed by SH, MM, CM, FC and CO. The first draft of the manuscript was written by SH and all authors commented on previous versions of the manuscript. All authors read and approved the final manuscript.

## Funding

Open access funding provided by University of the Western Cape. National Research Foundation, 101585, Mamogo Masenya.

## Data availability

The datasets generated during and/or analysed during the current study are available from the corresponding author on reasonable request.

## Declarations

**Conflict of interest** The authors have no relevant financial or non-financial interests to disclose.

**Open Access** This article is licensed under a Creative Commons Attribution 4.0 International License, which permits use, sharing, adaptation, distribution and reproduction in any medium or format, as long as you give appropriate credit to the original author(s) and the source, provide a link to the Creative Commons licence, and indicate if changes were made. The images or other third party material in this article are included in the article's Creative Commons licence, unless indicated otherwise in a credit line to the material. If material is not included in the article's Creative Commons licence and your intended use is not permitted by statutory regulation or exceeds the permitted use, you will need to obtain permission directly from the copyright holder. To view a copy of this licence, visit <http://creativecommons.org/licenses/by/4.0/>.

## References

1. C.V. Thompson, *Annu. Rev. Mater. Res.* **42**, 399 (2012)

2. F. Ruffino, M.G. Grimaldi, *Surf. Interfaces* **24**, 101041 (2021)
3. O. Kovalenko, J.R. Greer, E. Rabkin, *Acta Mater.* **61**, 3148–3156 (2013)
4. A. Sharipova, L. Klinger, A. Bisht, B.B. Straumal, E. Rabkin, *Acta Mater.* **231**, 117919 (2022)
5. W. Jiang, W. Bao, C.V. Thomson, D.J. Srolovitz, *Acta Mater.* **60**, 5578 (2012)
6. D.J. Srolovitz, S.A. Safran, *J. Appl. Phys.* **60**, 255–260 (1986). <https://doi.org/10.1063/1.337691>
7. F. Cheynis, E. Bussmann, F. Leroy, T. Passanante, P. Muller, *Phys. Rev.B* (2011). <https://doi.org/10.1103/PhysRevB.84.245439>
8. G.H. Kim, R.V. Zucker, J. Ye, W.C. Carter, C.V. Thompson, *J. Appl. Phys.* **113**, 043512 (2013). <https://doi.org/10.1063/1.4788822>
9. D. Amram, L. Klinger, E. Rabkin, *Acta Mater.* **60**, 3047–3056 (2012). <https://doi.org/10.1016/j.actamat.2012.02.009>
10. A. Bisht, Y. Qi, L. Klinger, E. Rabkin, *Acta Mater.* (2022). <https://doi.org/10.1016/j.actamat.2022.117984>
11. Y.J. Oh, J.H. Kim, C.V. Thompson, C.A. Ross, *Nanoscale* **5**, 401–407 (2013). doi:<https://doi.org/10.1039/c2nr32932h>
12. S. Pandit, S. Kunwar, P. Pandey, J. Lee, *Metals* **9**, 1011 (2019). doi:<https://doi.org/10.3390/met9091011>
13. M. Masenya, S. Halindintwali, M. Madhuku, M. Mtshali, F. Cummings, A. Shnier, D. Billing, D. Wamwangi, *Surf. Interfaces* **29**, 101783 (2022)
14. T. Kimoto, J.A. Cooper, *Fundamentals of Silicon Carbide Technology-Growth, Characterization, Devices, and Applications* (Wiley, Singapore, 2014)
15. M. Shur, S. Romyantsev, M. Levinshtein, *SiC Materials and Devices* (World Scientific Publishing, Singapore, 2007)
16. L.M. Porter, R.F. Davis, *Mater. Sci. Eng. B* **34**, 83–105 (1995)
17. R. Swanepoel, *J. Phys. E: Sci. Instrum. Vol 16*, 1214 (1983)
18. R. Swanepoel, *J. Phys. E: Sci. Instrum. Vol 17*, 896 (1984)
19. J. Tauc, in *Optical properties of Solids*, edited by F. Abelès (North-Holland, Amsterdam, the Netherlands) (1972), p. 277
20. S. Halindintwali, D. Knoesen, B.A. Julies, T. Muller, C.J. Arendse, *Amorphous and nc-Si: H intrinsic thin films for solar cells applications* (Materials Science ForumTrans Tech Publications, Switzerland, 2010), pp.191–207. <https://doi.org/10.4028/www.scientific.net/MSF.657.191>
21. W. Theiss 2001, [www.mtheiss.com](http://www.mtheiss.com)
22. Z. Du, C. Guo, X. Yang, T. Lui, *Intermetallics* **14**(5), 560–569 (2006)
23. G.L. Selman, P.J. Ellison, A.S. Darling, *Platinum Met. Rev.* **14**(1), 14 (1970)
24. X. Jia, Z. Lin, T. Zhang, B. Puthen-Veetil, T. Yang, K. Nomoto, J. Ding, G. Conibeer, I. Perez-Wurf, *RSC Adv.* **7**, 34244 (2017)

25. X. Chen, W. Zhou, Q. Feng, J. Zheng, X. Liu, B. Tang, J. Li, J. Xue, S. Peng, J. Nucl. Mater. **478**, 215–221 (2016)

**Publisher's Note** Springer Nature remains neutral with regard to jurisdictional claims in published maps and institutional affiliations.